

The initial spin matters: the impact of rapid rotation on magnetic-field amplification at merger

HARRY HO-YIN NG ,¹ JIN-LIANG JIANG ,^{1,2} AND LUCIANO REZZOLLA ,^{1,3,4}

¹*Institut für Theoretische Physik, Goethe Universität, Max-von-Laue-Str. 1, 60438 Frankfurt am Main, Germany*

²*Department of Astronomy, School of Physics and Astronomy, Key Laboratory of Astroparticle Physics of Yunnan Province, Yunnan University, Kunming 650091, People's Republic of China*

³*School of Mathematics, Trinity College, Dublin 2, Ireland*

⁴*CERN, Theoretical Physics Department, 1211 Geneva 23, Switzerland*

(Dated: January 23, 2026)

ABSTRACT

A couple of milliseconds after the merger of a binary system of neutron stars can play a fundamental role in amplifying the comparatively low initial magnetic fields into magnetar strengths. The basic mechanism responsible for this amplification is the Kelvin-Helmholtz instability (KHI) and we here report the first systematic study of the impact of rapid rotation on the KHI-amplification process exploiting general-relativistic magnetohydrodynamic simulations at very high-resolutions of 35 m. Concentrating on four different spinning configurations, we find that aligned, anti-aligned, and mixed (aligned/anti-aligned) spin configurations lead to markedly different growth rates of the electromagnetic (EM) energy, field topologies, and vortex properties when compared to the irrotational case. These differences arise from intrinsic variations in the system dynamics, such as tidal deformation, collision strength, and contact surface area, with the anti-aligned configuration producing the largest vorticity and growth in EM energy. Importantly, while different spin configurations lead to significantly different initial growth rates of the poloidal/toroidal components, all systems converge to a specific topological partition. Our simulations are confined to a short window in time, but the different EM energies produced as a result of spin will imprint the EM emission at merger and provide information on the spinning state at merger.

1. INTRODUCTION

Binary neutron star (BNS) mergers are rich multi-messenger events that emits gravitational waves (GWs) (Baiotti & Rezzolla 2017; Paschalidis 2017; Radice et al. 2020), and a large frequency range of electromagnetic (EM) signals, originated from magnetized flaring (Most & Quataert 2023; Musolino et al. 2025; Jiang et al. 2025), short gamma-ray burst (sGRB) due to the launching of relativistic jets (Giacomazzo et al. 2011; Rezzolla et al. 2011; Baiotti & Rezzolla 2017; Ciolfi 2020; Kiuchi et al. 2024; Gottlieb et al. 2023; Gottlieb et al. 2025; Chen et al. 2025), afterglow (Lyman et al. 2018; Hajela et al. 2019, 2022) and kilonova powered by the radioactive decay of *r*-process synthesised ejecta (Radice et al. 2016; Metzger 2017; Bovard et al. 2017; Zhu et al. 2022; Combi & Siegel 2023; Fujibayashi et al. 2023; Kawaguchi et al. 2023; Cheong et al. 2025; Ng et al. 2025).

The first multi-messenger BNS merger observed in 2017 provided both GW and EM detections (The LIGO Scientific Collaboration & The Virgo Collaboration 2017; Abbott et al. 2017; Fermi-LAT Collaboration 2017; Hajela et al. 2019). Due to the highly nonlinear dynamics of BNS mergers, intensive modelling with general-relativistic magnetohydrodynamics (GRMHD) simulations is required. A particularly challenging aspect is the accurate treatment of matter-magnetic field interactions. While these interactions are not expected to play a role in the inspiral (Giacomazzo et al. 2009; Zhu et al. 2020), they are crucial at merger and afterwards. Yet, despite significant progress in modelling magnetized BNS mergers (see, e.g., Mösta et al. 2020; Combi & Siegel 2023; Most et al. 2025; Fields et al. 2025; Celora et al. 2025), key MHD instabilities – such as the Kelvin-Helmholtz instability (KHI) and the magnetorotational instability (MRI) – remain difficult to fully resolve because of their strong sensitivity to grid resolution, making them computationally expensive to capture (see, e.g., Siegel et al. 2013; Palenzuela et al. 2022; Kiuchi 2024).

In particular, at merger the KHI can amplify the comparatively weak magnetic fields of the old and cold pre-merger neutron stars (NSs) by orders of magnitude and over a timescale that is of a couple of milliseconds only (Price & Rosswog 2006; Giacomazzo et al. 2015; Kiuchi et al. 2015; Chabanov et al. 2023; Kiuchi et al. 2024; Aguilera-Miret et al. 2025; Gutiérrez et al. 2025; Neuweiler et al. 2025). However, several issues regarding KHI-amplified magnetic fields remain unclear: (i) a saturated growth has not yet been

binaries	t_{mer} [ms]	$t_{\text{sh}} - t_{\text{mer}}$ [ms]	$t_{\text{sh},1/2} - t_{\text{mer}}$ [ms]	t_{KHI} [ms]	v_a [c]
IR	51.6	-0.06	0.63	0.69	0.013
UU	57.0	-0.01	1.34	1.35	0.010
DD	34.4	-0.32	0.69	1.01	0.040
DU	44.6	-0.49	0.52	1.01	0.026

Table 1. Summary of the relevant times for the four binaries simulated: irrotational IR, aligned UU, anti-aligned DD, or mixed DU. Reported are: the merger time t_{mer} , the “shear time” t_{sh} when the KHI develops robustly (i.e., when the growth rate γ is $\gamma = \gamma_{\text{max}}/3$, where γ_{max} is the maximum growth rate), the “half-time” $t_{\text{sh},1/2}$ when the KHI can be considered globally quenched (i.e., when $\gamma = \gamma_{\text{max}}/2$ and γ_{max} have both been reached), the KHI duration time $t_{\text{KHI}} := t_{\text{sh},1/2} - t_{\text{sh}}$, and the approaching velocity v_a of the maximum rest-mass density when the two NSs have a separation of $18 M_{\odot}$.

achieved, except in the large eddy simulations (LES) employing phenomenological subgrid models (Aguilera-Miret et al. 2024; Aguilera-Miret et al. 2025); (ii) the influence of the initial magnetic-field topology and magnetic field strength (Chabanov et al. 2023; Jiang et al. 2025; Gutiérrez et al. 2025; Cook et al. 2025); (iii) the impact of the initial conditions in terms of the masses, mass ratio, NS spins, and equation of state (EOS) (Dudi et al. 2022; Bamber et al. 2024; Musolino et al. 2025; Neuweiler et al. 2025).

While direct simulations that have so far represented the most robust way to explore these issues, progress on any of them has been hindered by the enormous computational costs. We here address in part point (iii) by exploiting a novel “hybrid” approach which reduces significantly the computational costs by making use of two GRMHD codes optimized for different phases (inspiral/merger) of BNSs (Jiang et al. 2025). In this way, we are able to use very high resolutions of 35 m on rather large portions of the domain and, at the same time, consider a coarse but broad sampling of the space of parameters. In this way, we can assess how the initial spin affects both the amplification process and the properties of the turbulence generated during the merger and early post-merger phases.

2. NUMERICAL SETUP

The simulations reported below are obtained by applying hand-off procedure developed in Ng et al. (2024), and employed in Jiang et al. (2025), which focus on the BNS postmerger stage. In essence, a hand-off procedure consists of the exchange of data between two GRMHD codes, `FIL` (Most et al. 2019, 2020), which solves the full set of Einstein equations with the constraint-damping formulation of the Z4 formulation (Bernuzzi & Hilditch 2010; Alic et al. 2012) and `BHAC+` (Ng et al. 2024; Jiang et al. 2025), which solves the Einstein equations under the conformal flatness condition (CFC) (Cordero-Carrión et al.

2009; Bucciantini & Del Zanna 2011; Cheong et al. 2021) together with a new gravitational-wave radiation-reaction (GWRR) treatment (Jiang et al. 2025) improving previous formulations (Faye & Schäfer 2003; Oechslin et al. 2007). Both codes employ a fourth-order accurate conservative finite-difference scheme with a WENO-Z reconstruction method (Acker et al. 2016; Most et al. 2019) coupled with an HLL Riemann solver (Harten et al. 1983; Rezzolla & Zanotti 2013). While `FIL` employs a vector-potential based constrained transport scheme (Etienne et al. 2015), `BHAC+` uses a magnetic-field based upwind constrained transport (Olivares et al. 2019). Both codes use a third-order Runge-Kutta method for the time integrator with a Courant-Friedrichs-Lowy (CFL) factor of $\mathcal{C}_{\text{CFL}} = 0.2$ and Cartesian coordinates with a reflection symmetry on the $z = 0$ plane; it was recently shown that this symmetry is accurately preserved in the first ms after merger (Gutiérrez et al. 2025).

To explore the impact of the stellar spin on the magnetic-field amplification by KHI, we construct equal-mass rapidly spinning BNS configurations having the same total mass of $2.584 M_{\odot}$, initial separation of $38 M_{\odot}$, and being governed by temperature-dependent TNTYST EOS (Togashi et al. 2017). The initial binaries are in quasi-circular equilibrium and computed with the open-source code `FUKA` (Papenfort et al. 2021; Tootle et al. 2021) and each star has a dimensionless spin $\chi := J_s/M^2 = 0.35$, where M and J_s are respectively the gravitational mass and spin angular momentum, with the latter being parallel to the orbital angular momentum J . For our EOS, this corresponds to a rotation frequency of 620 Hz, which is smaller than the largest observed frequency of 716 Hz ($\chi \sim 0.4$) for PSR J1748–2446ad (Hessels et al. 2006). To cover the possible space of parameters, we consider four configurations that are distinguished by the spin orientation, i.e., binaries that are either: irrotational IR, aligned UU, anti-aligned DD, or mixed DU (see Table 1 for a summary)

Because of different mesh-refinement strategies [moving boxes in `FIL` Schnetter et al. (2004) and quadtree–octree blocks in `BHAC+` (Porth et al. 2017; Keppens et al. 2021)], the grid setup is different in the two codes. More specifically, the `FUKA` initial data is first evolved by `FIL`, with the outer boundary set at $1000 M_{\odot}$ and employing six refinement levels. The finest refinement level encompasses a box region of $[-16, 16] M_{\odot}$ ($[-23.6, 23.6]$ km) in each direction with a finest resolution of 300 m. In all simulations, a weak and purely poloidal magnetic field is introduced in each star slightly before the merger (i.e., at time $t - t_{\text{mer}} \simeq -1.2$ ms) and its strength is adjusted such that all stars have the same maximum magnetic-field strength of $|B|_{\text{max}} \simeq 3.8 \times 10^{11}$ G in the Eulerian frame [see coefficient A_b in Eq. (15) in Jiang et al. (2025)]; in all cases, the magnetic-dipole vector and the spin angular-momentum vectors are parallel (see also Kawa-

mura et al. (2016); Ruiz et al. (2018, 2020) for previous work with different magnetic-field orientations). Because stars magnetized in this way do not correspond to consistent solutions of the GRMHD system (see, e.g., Bonazzola & Gourgoulhon 1996; Frieben & Rezzolla 2012; Chi-Kit Cheong et al. 2024, for examples of consistent solutions), the “late” magnetization of the star is made to avoid artificial amplification/dissipation of magnetic fields due to inconsistencies between initial data and magnetic fields.

The large initial separation of ~ 56 km – necessary to obtain convergence when considering such high initial spins – also leads to a large number of inspiral orbits before merger (i.e., between 9 for the DD and 15 for the UU configurations) that are computed by the `FIL` code. Right before the formation of the shearing layer and the occurrence of KHI ($t - t_{\text{mer}} \simeq -1$ ms), the hand-off to `BHAC+` takes place, with a change in the outer boundary from $2000 M_{\odot}$ (in `FIL`) to $100 M_{\odot}$ (in `BHAC+`) and an increase to eight refinement levels, thus having the finest resolution of 35.0 m. We note that even higher resolutions of 12.5 m have been used in the recent past (see, e.g., Kiuchi et al. 2024) on volumes smaller than those we covered at 35 m corresponding to a cubic box of extent $[-12, 12]$ km. Our experience with very high resolutions restricted to small volumes has revealed that this can lead to artifacts that can easily go unnoticed. To avoid them, and keep the computational costs comparable, we have decreased the resolution to 35 m but increased the volume covered.

Obviously, the hand-off implies a change in the way the Einstein equations are solved and comes with a number of advantages and one (minor) disadvantage. First, the CFC scheme(s) has been used with success to study core-collapse supernovae (Dimmelmeier et al. 2002; Ott et al. 2007), isolated NSs (Yoshida 2012; Ng et al. 2021; Yip & Li 2025), and even BNS mergers (Oechslin et al. 2007; Bauswein & Stergioulas 2015). More recently, Jiang et al. (2025) have also shown that an improved CFC scheme – the extended CFC (xCFC) complemented with GWRR terms – recovers with high accuracy a full general-relativistic description of the remnant of a binary merger. Second, the timestep can be set to be much larger than in a full numerical-relativity code since it is no longer limited by the speed of light but by the speed of sound. Third, the solution of the set of elliptic xCFC constraint equations does not need to be computed at every timestep but at a fraction of the GRMHD timesteps. When combined, these advantages lead `BHAC+` to have a net saving of $\sim 80\%$ of the computational costs to be sustained by `FIL` (Jiang et al. 2025). At the same time, the basic xCFC scheme does not account for energy and momentum losses via GWs. These losses can be included with the GWRR corrections, which then yield evolutions that reproduce very well the bulk dynamics of full general-relativistic simula-

tions. Furthermore, these losses are not the main source of error, which remains in the finite resolution of the simulations (the relative difference between the xCFC solution and the full numerical-relativity solution is $\sim 3\%-12\%$; see appendix B for more details).

In summary, we find that the substantial reduction in computational cost and the ability to carry out a broad investigation of the space of parameters employing very high resolutions that would be otherwise unsustainable, shadows the relatively small errors introduced by the approximate gravitational description.

3. RESULTS

3.1. Spins, KHI and Shocks

Being an instability, the KHI will be characterised by an exponential behaviour in time, so that, dynamical quantities such as the total EM energy E_{EM} [see Eq. (A3) in Jiang et al. (2025) for a definition] will have a dynamical behaviour of the type $E_{\text{EM}} \sim (E_{\text{EM}})|_{t=t_{\text{sh}}} \exp(\gamma t)$, where $\gamma := \dot{E}_{\text{EM}}/E_{\text{EM}}$ is the growth rate and t_{sh} is the “shear time”, i.e., the time when the exponential behaviour is first recorded. In a linear regime and under idealised conditions, γ is assumed to be a constant; however, in the highly nonlinear conditions in which the KHI develops at a BNS merger, the growth rate is actually time dependent, $\gamma = \gamma(t)$, and it is therefore useful to introduce t_{sh} and $t_{\text{sh},1/2}$ respectively as the times when γ reaches either $1/3$ or $1/2$ of its maximum value on either side of it [i.e., $t_{\text{sh}} (t_{\text{sh},1/2})$ marks the time when $\gamma = \gamma_{\text{max}}/3 (\gamma = \gamma_{\text{max}}/2)$ before (after) the maximum value γ_{max} is reached]. Within this notation, t_{sh} and $t_{\text{sh},1/2}$ can be taken to define the effective times when the KHI robustly develops and is globally quenched, respectively. We remark, however, that these serve mostly as reference times among the various spinning configurations and it is possible that the KHI is locally active before t_{sh} and after $t_{\text{sh},1/2}$. These two times are useful to compare the growth rates across the various cases considered and to determine a window in time during which the KHI is robustly active. In the presence of spin, in fact, an artificial linear growth is measured even before the NSs enter in contact, hence the need for t_{sh} for approximately indicating the starting moment of exponential growth and the formation of shear layer. The magnetic field is still growing rapidly because of the turbulent amplification following the KHI, hence the need for introducing $t_{\text{sh},1/2}$ (see also Chabanov et al. 2023, for a more extended discussion). The values of t_{sh} and $t_{\text{sh},1/2}$ are reported in Tab. 1.

Figure 1 shows, relative to t_{sh} and for the four binaries considered here, the evolutions of the total EM energy E_{EM} (top panel), of its poloidal and toroidal components $E_{\text{EM}}^{\text{pol}}$, $E_{\text{EM}}^{\text{tor}}$ [second panel from the top; see Eqs. (A3)–(A5) in Jiang et al. (2025) for a definition], the evolution of the total growth

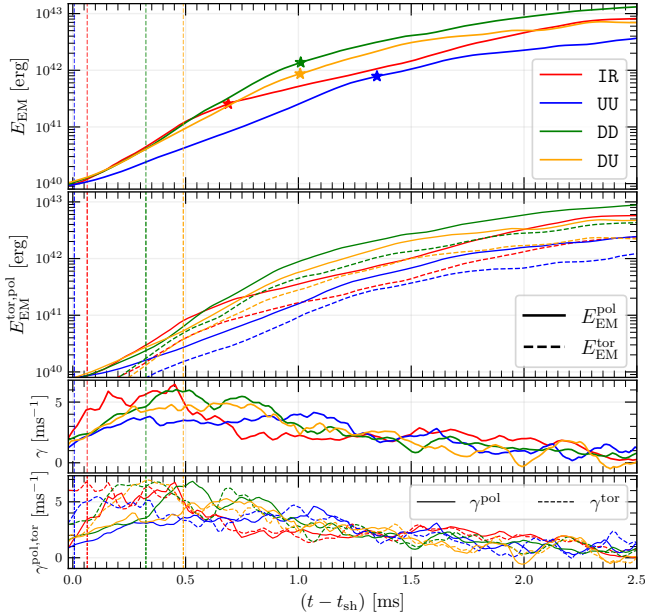


Figure 1. *Top panel:* evolution of the total EM for the four binaries considered, star symbols indicating when the KHI can be considered to be globally quenched ($t = t_{\text{sh},1/2}$). *Second panel:* evolutions of the EM energy in the poloidal (solid lines) and toroidal components (dashed lines). *Third panel:* Evolutions of the KHI growth rate $\gamma := \dot{E}_{\text{EM}}/E_{\text{EM}}$. *Bottom panel:* evolutions of the KHI growth rates in the poloidal (solid lines) and toroidal components (dashed lines). In all panels, the vertical dashed lines mark the merger time t_{mer} for each binary.

rate γ (third panel), and of the various components (bottom panel); all energies are computed over the whole computational domain for all configurations in Tab. 1.

A number of considerations can be made after analysing Fig. 1. The first, and possibly most important in our study, is that the “*initial spin matters*”, namely, the KHI-induced amplification of the magnetic field and the subsequent turbulent amplification are strongly influenced by the spin of merging stars. This can be appreciated from the top panel of Fig. 1, which shows how the binary with aligned spins, i.e., the UU binary, has the lowest EM magnetic energy at the end of the time interval considered and among all cases considered. By contrast, the binary with anti-aligned spins, i.e., the DD binary, has the highest EM energy, which is ~ 5 times larger than for the UU binary. Interestingly, the mixed-spin binary, i.e., the binary DU, has a final EM energy that is comparable with that of the irrotational binary IR even though the evolution is rather different.

Second, note the complex relation between the merging time t_{mer} and the time at which the KHI starts developing robustly, t_{sh} . While the DD binary is the first to merge and

the UU binary the last one¹, the binaries DU and IR follow in this order (see the dashed vertical lines in the top panel, which mark t_{mer} and Tab. 1). These differences in the times of shear emerge because the exponential increases in EM energy occur earlier for the two binaries with an anti-aligned NS (i.e., with an earlier t_{sh}), as these stars are more strongly tidally deformed during the late-inspiral phase due to larger spin-dependent dynamical tidal effects and counter-rotation of the down-spin star relative to the orbital motion (see Steinhoff et al. 2021, for details).

Third, the poloidal component of the EM energy (solid lines in the second panel from the top) is about twice that of the toroidal component (dashed lines) and this ratio is very similar for all cases after $t_{\text{sh},1/2}$, which are marked with coloured stars (see also below for a detailed discussion).

Fourth, the growth rates of the KHI are also rather different in the four cases and during the course of the evolution. Interestingly, the irrotational IR binary has the largest initial growth rate (see third panel from the top), while the UU binary has the smallest one. At late times, i.e., for $t > t_{\text{sh},1/2}$ and when the KHI has been quenched, the growth rates are remarkably similar in all four binaries.

Fifth, after the KHI stage ends and before the winding and MRI phases, all cases enter a turbulent amplification stage (Siegel et al. 2013). This stage represents nonlinear amplification driven by interactions among KHI-induced small-scale eddies and the reorganisation of the fluid prior to reaching a quasi-equilibrium state. Although the growth rate during this stage is lower than in the KHI phase, it helps counteract EM energy attenuation caused by strong pressure gradients resulting from core contraction and expansion, mass ejection, and numerical resistivity. Finally, and not surprisingly, the initial growth rates of the toroidal components are the largest but not much larger than those of the poloidal ones (see fourth panel from the top).

In order to understand why and how the different spin configurations influence the magnetic-field amplification via the KHI, it is useful to study the equatorial distribution of the magnetic field strength $|B| := \sqrt{B^i B_i}$ and the associated vortical structure. This is reported in Fig. 2 for all binaries (different rows) and at times t_{sh} , $t_{\text{sh},1/2}$, and $t - t_{\text{sh}} = 2$ ms (different columns). For a more detailed comparison of the properties of the KHI-unstable shear layer when the two stars come into contact, we have rotated the distributions for the IR, UU, and DD cases so that the maxima of the rest-mass density ρ of the two NSs at $t = t_{\text{sh}}$ (first column) are on the $y = 0$ line. On the other hand, for the DU binary, where

¹ The delay in the merger time with increasing spin is also known as the “hang-up” effect and reflects the spin-orbit angular-momentum interaction appearing already at the 1.5 post-Newtonian (PN) order (see, e.g., Blanchet 2014).

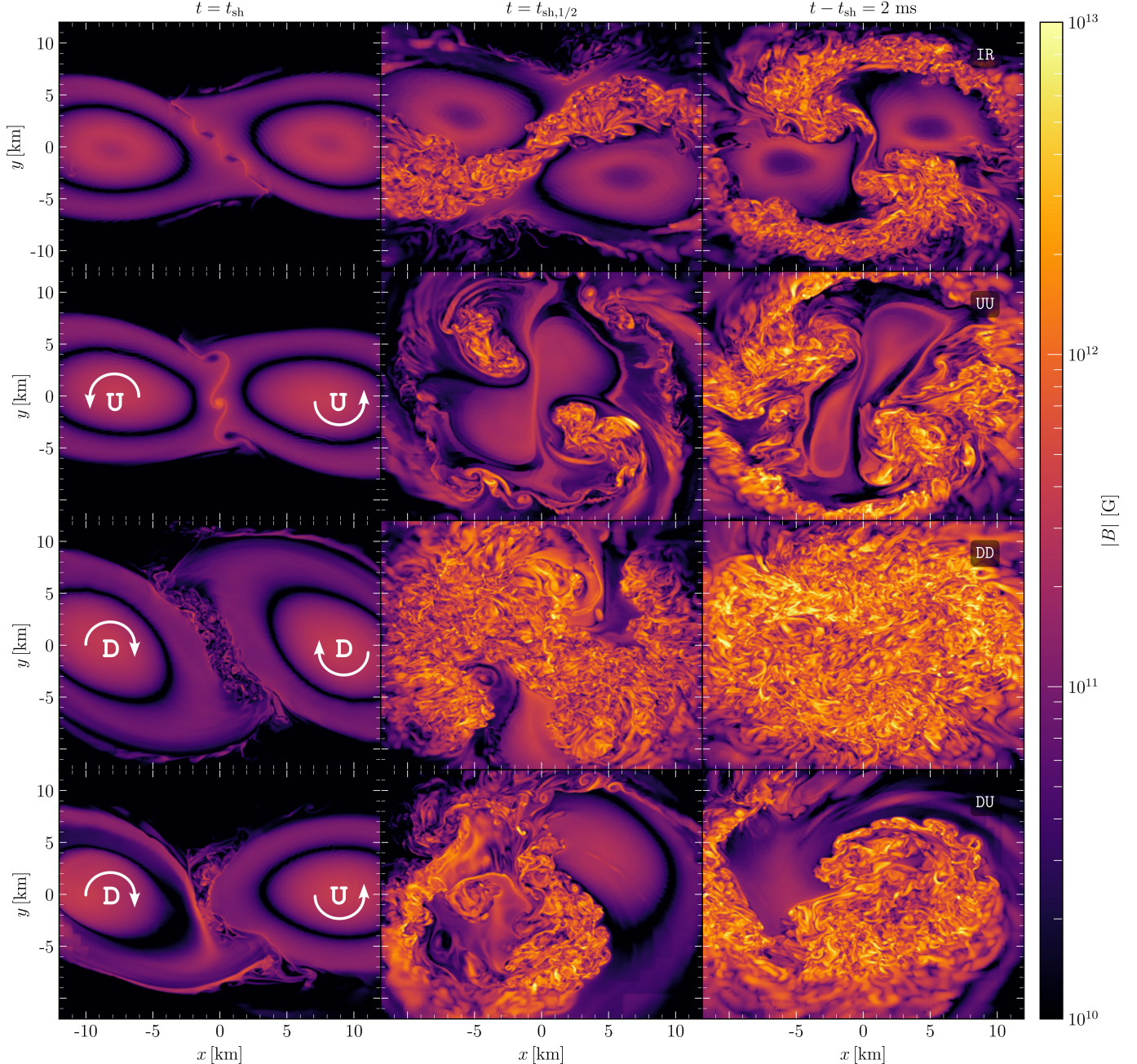


Figure 2. Distributions of the magnetic-field strength $|B|$ on $z = 0$ -plane for all cases considered (different rows) at times $t = t_{\text{sh}}$, $t_{\text{sh},1/2}$, and $t - t_{\text{sh}} = 2$ ms (different columns). Note that all figures have been rotated so that the maxima of the rest-mass density of the two NSs at $t = t_{\text{sh}}$ are on the $y = 0$ line (for the DU binary, only the density maximum of aligned-spinning star is on $y = 0$ line.). Each panel reports data covered by the finest resolution box with $\Delta x \simeq 35$ m. The arrows in first column indicate the spin-alignment of each star.

one component is tidally disrupted (see below), the rotation is made such that only the rest-mass density maximum of the star with aligned spin is on the $y = 0$ line.

The different columns in Fig. 2 are chosen so as to contrast the evolutions at three important times. More specifically, the first column, at $t = t_{\text{sh}}$, illustrates the stellar shapes at the onset of the shear layer and vortices. The second column, at $t_{\text{sh},1/2}$, marks the end of the KHI, as that this time

the normalized growth rate drops to half of its peak value. At this stage, the KHI-driven eddies have expanded and been advected into wider regions of the remnant, and in some configurations they even penetrate into the deeper stellar interior. The third column, at $t - t_{\text{sh}} = 2$ ms, represents a time that is close to the end of the simulated window, where the KHI stage has concluded and the subsequent turbulent amplifica-

tion has begun, but before the winding and MRI stages. We will next discuss in detail the evolution in these three stages.

Hence, the first column in Fig. 2 allows one to observe the preliminary contacts between the tidally disrupted low-density shear layers in the DD and DU cases. Note therefore that the KHI can develop already early-on and in low-density matter; this result modifies the expectation that shear layers prone to the KHI form primarily in high-density regions, whereas the Rayleigh-Taylor instability occurs in low-density matter (Palenzuela et al. 2022). We should also note that these early exponential growths by the KHI are not observed in low-resolution simulations, indicating that, given sufficiently high resolution, strong spin-induced dynamical tides can trigger an earlier KHI phase. Specifically, in the DU configuration, the tidal forces acting on the anti-aligned-spin star are stronger than those on the aligned-spin star, causing it to plunge into its companion and generate a shear layer earlier than in all other binaries. Another aspect that can be appreciated from the first column of Fig. 2 is that the contact surface area can be quite different and is systematically larger for the configurations involving down-spin star(s). Indeed, at the moment the shear layer forms, only the stellar tips begin to touch in the IR and UU cases. By contrast, for the DD and DU configurations, which experience stronger tidal deformations, the stellar bodies of two NSs contact each other, resulting in a significantly larger stellar surface area being involved in the collision.

Proceeding in time, the second and third columns of Fig. 2 gives a revealing representation of the magnetic-field distribution around the moment of merger and when the KHI has been quenched. In this way, it is possible to appreciate that the DD binary (third row), which can benefit from a number of favourable factors, such as the highest approaching velocity v_a resulting from the smallest angular-momentum loss (“hang-up” effect) the smallest total angular momentum (see the values of v_a in Tab. 1 and the discussion in Fig. 3), an earlier tidal shearing, a larger contact surface area, and a larger discontinuity in the tangential velocities (see arrows in Fig. 2) can lead to a very strong vorticity, with eddies being produced in both the high- and low-density regions. More importantly, the vorticity pervades all regions of the NSs, penetrating down to the highest-density cores. This behaviour should be contrasted with that reported for the traditional irrotational binary IR (first row), where it is apparent that the vorticity at this stage in the evolution is confined to the low-density regions of the two stars (see also Fig. 2 of Chabanov et al. 2023, for a snapshot at a later time). On the other extreme, the UU binary (second row) has properties that are the opposite of those illustrated for the binary DD and thus develops a much weaker vorticity as a result of milder kinetic conditions at the time of the merger (see also Neuweiler et al. 2025), with significant velocity gradients ap-

pearing only when the high-density regions collide. Indeed, the UU binary exhibits the longest inspiral and the strongest GW emission, which results in a deficit of both kinetic and internal energies, producing the few and weak eddies and ultimately forming a colder remnant (see also Karakas et al. 2025). Given the very different conditions at merger, it is not surprising that the DD/UU binaries lead to the largest/smallest overall growth in the EM energy right after KHI phase.

A special discussion should be reserved for the DU binary (fourth row), where the turbulence is initially developed and is restricted only to the NS with anti-aligned spin (a similar behaviour is shown in Fig. 1 of Aguilera-Miret et al. 2025, although a detailed discussion is not presented). To understand the origin of this behaviour, it is useful to recall that the NS with anti-aligned spin is severely tidally deformed during the late inspiral and that the material that is stripped forms a strong shear layer surrounding the NS with aligned-spin. (see also Fig. 3). In turn, this leads to a very asymmetrical flow and vorticity distribution which leads to the behaviour described in the last row of Fig. 2. As a result, although the DU binary has the second-largest approaching velocity and generates a significant fraction of vortices during the early phase of the tidal shearing, the large asymmetry in the flow prevents a direct collision between the two NSs and an efficient KHI development. The asymmetry also disrupts the shear layer and very effectively suppresses the development of eddies. This behaviour also explains why the growth of the EM energy in the IR binary becomes larger than that of the DU binary at later times (see top panel of Fig. 1).

The variations in behaviours among all cases discussed, such as the collision strength, the tidal dynamics, and the contact area, clearly reveal that, when sufficiently high resolutions are employed, different spin configurations create intrinsically different dynamics and substantially contrasting environments for the development of KHI-driven eddies. The fact that the early post-merger phase is sensitive – in addition to spin – also to distinct magnetic-field configurations or strengths (Chabanov et al. 2023; Gutiérrez et al. 2025), is not necessarily in contrast with the suggestion that a quasi-universal postmerger magnetic-field state will be reached at sufficiently high resolutions (see, e.g., Aguilera-Miret et al. 2022). It is indeed possible that much of the initial conditions – although not all of them – will be washed out if the evolution takes place for sufficiently long timescales. What is relevant to remark, however, is that we clearly show that initial spins – more than the initial magnetic-field – can largely alter the intrinsic dynamics of the system and drive different strength/population of KHI eddies, which are not affected by simply changing the magnetic-field strength and topology. Therefore, our results could form the postmerger remnants with significantly different saturated states as a result of the different developments of the KHI. In turn, the different

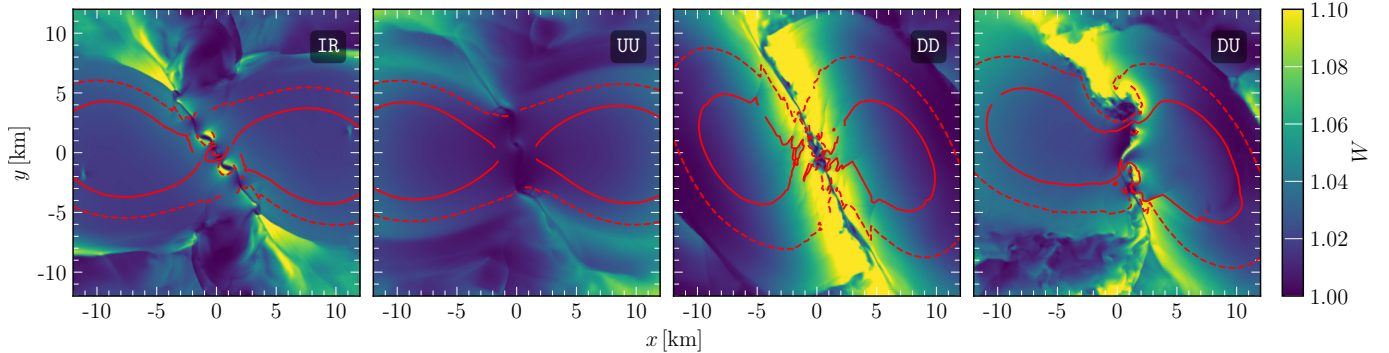


Figure 3. Distributions of the Lorentz factor W for all cases considered (different columns) at time $t = t_{\text{mer}}$. As in Fig. 2, the distributions are rotated so that the stellar centres are on a $y = 0$ line. Dashed and solid lines correspond to the rest-mass density contours of 4×10^{14} and $6 \times 10^{14} \text{ g cm}^{-3}$, respectively.

magnetic-field amplifications can lead EM emission in this time-frame that will be obviously different.

As anticipated above, the initial spin in the two stars regulates the angular momentum of the system at merger and thus determines the amount of kinetic energy with which the two stars collide. In turn, the different speeds at which the star shear – and the strength of the shocks resulting from the collision – will play a fundamental role in shaping the vorticity and thus the efficiency of the KHI in amplifying the magnetic field in the four scenarios considered. In this sense, the magnetic-field amplification shown in Fig. 1 reflects the combined effects of collision properties, the extent of vorticities generated, and the survival time of the shear layer.

To illustrate the role played by shocks at merger, Fig. 3 shows the Lorentz factor in the Eulerian frame W at time $t = t_{\text{mer}}$, together with isocontours of the rest-mass density to represent distribution of rest-mass as the two NSs collide. Taking the distribution of the Lorentz factor as a proxy for the strength of the shocks at merger, Fig. 3 explains why the UU binary experiences the longest KHI but also has the lowest magnetic-field magnification. This is because, at merger, this binary generates the weakest vorticity but also experiences the weakest shocks after collision (second panel from the left). By contrast, the NSs in the DD binary approach with a large kinetic energy, produce very strong shocks (second panel from the right) and these can expose the dense regions of the stars – that are obviously endowed with the strongest magnetic fields – to the vorticity of the KHI.

From Fig. 3 it is also possible to appreciate the special nature of the DU binary (right panel), which experiences an asymmetric but strong shock at collision. This behaviour, together with the strong but limited vorticity discussed in Fig. 2, leads to a large decay in the growth rate (see Fig. 1), giving this binary – together with DU – the shortest lifetime among those with nonzero spin. Finally, also noticeable in Fig. 3 is the different extents of the surface areas at contact. In particular, note how all stars with an anti-aligned spin (DD and DU) exhibit substantially larger contact surface areas. By

contrast, the binary with aligned spins (UU) has the smallest effective surface at the time of the collision.

Finally, Fig. 3 also helps in understanding the differences in the duration of the KHI, which is the result of the interplay between the generated shocks, the survival time of the shearing region, and the strength and extent of the vorticity eddies. Table 1 reports the KHI duration time, which is defined as $t_{\text{KHI}} := t_{\text{sh},1/2} - t_{\text{sh}}$, and it is then possible to realise that the UU binary, which we have already commented leads to the weakest amplification, also experiences the longest-lasting KHI ($t_{\text{KHI}} = 1.35 \text{ ms}$). On the contrary, the DD binary, which leads to the strongest amplification has a rather short-lived KHI ($t_{\text{KHI}} = 1.01 \text{ ms}$). Interestingly, while the IR binary exhibits the second strongest collision strength (excluding the special DU case), it possesses the shortest-lived KHI. This is mostly because it lacks the the extended period of early shearing driven by the strong dynamical tidal effects present in anti-aligned spin configurations.

3.2. On the Topological Equipartition

The study of vorticity in BNS mergers has a long history [see, e.g., Fig. 5 of Rasio & Shapiro (1999), Fig. 3 of Price & Rosswog (2006), or Fig. 16 of Baiotti et al. (2008)] and has a direct impact on the evolution of the topological components of the magnetic field, i.e., the toroidal and poloidal one. Given the purely (or predominantly) poloidal nature of the initial magnetic field and the predominantly toroidal nature of the flow before merger, the induction equation in ideal MHD trivially predicts the growth of the toroidal component. Indeed, this is also what is recorded in Fig. 1, whose fourth panel from the top shows how the toroidal component has the largest growth rate initially right after the formation of shear.

Yet, also the poloidal component of the magnetic energy grows of three orders of magnitude from the initial values and this is less obvious to account for. Palenzuela et al. (2022) and Kiuchi et al. (2024) briefly note that KHI-induced small-scale turbulence is isotropic, amplifying magnetic fields in random orientations and thereby producing similar growth

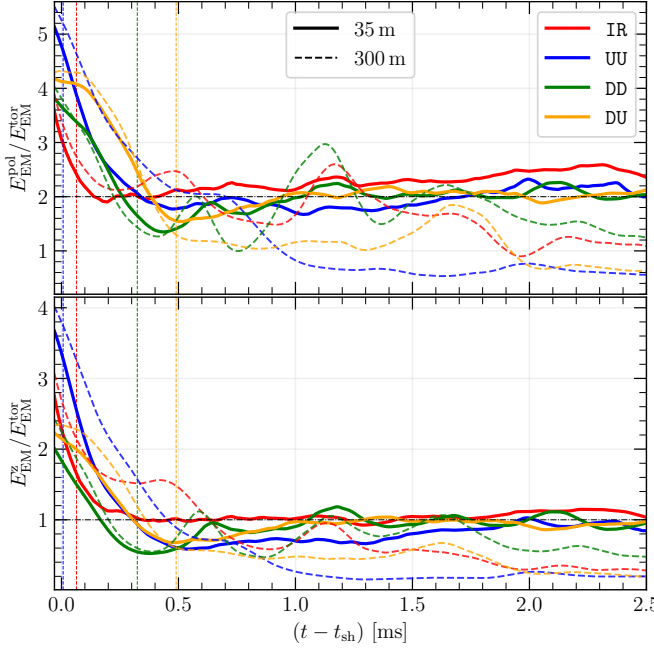


Figure 4. *Top panel:* evolution of the ratio of the EM energy in the poloidal and toroidal components (solid lines) for all binaries considered; note that at late times the ratio converges to a constant value of $\simeq 2$. *Bottom panel:* as in the top but relative to the ratio between the z - and the toroidal components; note that at late times the ratio converges to a constant value of $\simeq 1$. Shown with dashed lines are the same quantities when employing a coarser resolution of 300 m and yielding to significantly different values.

rates for both poloidal and toroidal components. While this is correct as a first approximation, it does not explain why the growth rates of the toroidal and poloidal components are offset in time, with the latter (former) prevailing at later (earlier) times. As we discuss below, this behaviour can be understood because the KHI-induced eddies are initially anisotropic – i.e., confined to specific regions of the star where the shearing takes place – and only later spread to the stellar interior, with the initial spins playing an important role in determining when the transition to isotropy takes place. Furthermore, after the transition has taken place, there is no topological equipartition between the toroidal and poloidal components, i.e., $E_{\text{EM}}^{\text{pol}}/E_{\text{EM}}^{\text{tor}} \neq 1$, although there is an equipartition in the vertical and horizontal directions for all binaries considered, despite their dynamics is considerably different.

To illustrate this finding, we show in Fig. 4 the evolution of the ratio between the EM energy in the poloidal and toroidal components $E_{\text{EM}}^{\text{pol}}/E_{\text{EM}}^{\text{tor}}$ (top panel), as well as of the ratio between the vertical [i.e., in the z -direction when adopting a decomposition in cylindrical coordinates (ϖ, ϕ, z)] and the horizontal (i.e., toroidal) components $E_{\text{EM}}^z/E_{\text{EM}}^{\text{tor}}$ (bottom panel). We note that the vertical component is produced by the generation of vertical vortices at the time of contact of the high-density regions (see also Appendix A) and that this

component is generated at different times for different binaries. In particular, this poloidal component will grow after the toroidal one and as a result of shearing away from the equatorial plane (see also bottom panel of Fig. 1). Lines of different colour refer to the different binaries, and solid lines are used to report the results of the high-resolution simulations (35 m), while the dashed lines refer to the low-resolution ones (300 m); here too, the vertical dashed lines mark t_{mer} .

Collecting the information in the two panels of Fig. 4, it then becomes clear that when the KHI has been quenched, for all four binaries $E_{\text{EM}}^{\text{pol}} \sim 2E_{\text{EM}}^{\text{tor}}$, but also that

$$E_{\text{EM}}^{\varpi} \approx E_{\text{EM}}^z \approx E_{\text{EM}}^{\text{tor}} \approx E_{\text{EM}}^{\text{pol}}/2, \quad (1)$$

where we recall that $E_{\text{EM}}^{\text{pol}} := E_{\text{EM}}^{\varpi} + E_{\text{EM}}^z$. In other words, after the KHI has ended, equipartition in all magnetic-fields components is reached and the poloidal component will always be twice as large as the toroidal component. Importantly, this result, i.e., the equivalence between E_{EM}^z and $E_{\text{EM}}^{\text{tor}}$, can be attained only when sufficiently large resolutions are used, because low-resolution simulations do not show a common behaviour (dashed lines in Fig. 4).

4. CONCLUSIONS

Assessing if and how the comparatively low magnetic fields of $\sim 10^8 - 10^{10}$ G characterising two NSs before their merger are amplified to magnetar-strengths of $\sim 10^{15} - 10^{16}$ G only a couple of milliseconds after merger represents one of the most important aspects of the dynamics of BNS systems and remains only poorly understood. The enormous computational costs associated with the direct numerical simulations that can probe reliably this process have so far prevented an exhaustive investigation of the impact that the initial spins have on the merger dynamics and on the development of the Kelvin-Helmholtz instability (KHI).

Leveraging on general-relativistic magnetohydrodynamic simulations at very high-resolution of 35 m and on a novel strategy exploiting the combined approach of two numerical-relativity codes, we have here reported the first systematic study of how rapid rotation impact the KHI-amplification process. The strategy consists of employing a numerical-relativity GRMHD code for the solution at comparatively smaller resolutions of the full set of Einstein equations in the (long) inspiral phase and to “hand-off” the data over to different code that can solve them in the xCFC approximation at much higher resolutions. While this approach is still computationally challenging, it yields a substantial computational saving that makes a systematic investigation as this one effectively possible.

To explore sparsely but broadly the space of parameters, we have considered four different spinning configurations that include, besides a standard irrotational binary, also binaries with rapid spin configurations that are either aligned,

anti-aligned, aligned/anti-aligned (mixed) with respect to the orbital angular momentum. In this way, and contrary to previous expectations deduced at much lower resolutions that the spin contributions would not affect the KHI, we have found that the KHI-induced amplification of the magnetic field, which represents only a portion of the window in time covered by the simulations, is strongly influenced by the spin of merging stars.

More specifically, the binary with aligned spins (UU) has, at the end of the simulations, the lowest EM energy considered among all cases considered. By contrast, the binary with anti-aligned spins (DD) has an EM energy that is ~ 5 times larger than for the UU binary and is the largest of the ones found. Interestingly, even though the evolution is rather different, the mixed-spin binary (DU) has a final EM energy that is comparable with that of the irrotational binary (IR).

These differences are the consequence of a number of intrinsic variations in the system dynamics, which include: the tidal deformation before merger, the jump in the tangential velocity – and hence the vorticity – at contact, the shock strength at the collision, and the extent of the surface area involved in the KHI. At the cost of oversimplifying, the role of spin in the development of the KHI can be summarised as follows: in order to obtain a strong magnetic-field amplification via the KHI it is necessary to have both strong shocks (that can expose strong magnetic fields) and strong vorticity (that can mix them efficiently). The DD binary experiences both strong shocks and strong vorticity, and is thus the most efficient amplifier. The DU binary experiences strong shocks but has an asymmetric vorticity, which reduces the efficiency in the amplification. The UU binary experiences neither strong shocks nor strong vorticity, making it the least efficient magnetic-field amplifier among the configurations considered.

Our simulations, and the high-resolutions at which they are performed, also reveal that despite the fact that different spin configurations yield significantly different initial growth rates of the poloidal/toroidal components, all binaries converge to a precise topological partition as a result of the formation of vertical vortices, advection and cascade of the EM energy in small-scale eddies. More specifically, after the KHI has ended, the poloidal component of the EM energy is always twice as large as the toroidal one, with true equipartition being reached only in the three components of the magnetic field.

It is possible that the dynamics described here – and in particular the topological equipartition – is in large part “quasi-universal”, that is, largely independent of the system properties, such as the EOS, the mass ratio, the initial magnetic-field and the binary eccentricity. This is because, for sufficiently high rotation, the spin-induced corrections discussed here in the development of the KHI will remain the most im-

portant in the budget of possible effects influencing the KHI. New simulations that are longer, explore different mass ratios and EOSs, and include neutrino transport are necessary to confirm this conjecture.

1 It is a pleasure to thank M. Cassing, M. Chabanov, E. R.
 2 Most, and K. Topolski for useful discussions. This research
 3 is supported by the ERC Advanced Grant “JETSET: Launch-
 4 ing, propagation and emission of relativistic jets from bi-
 5 nary mergers and across mass scales” (grant No. 884631),
 6 by the Deutsche Forschungsgemeinschaft (DFG, German
 7 Research Foundation) through the CRC-TR 211 “Strong-
 8 interaction matter under extreme conditions” – project num-
 9 ber 315477589 – TRR 211. L.R. is grateful to the Theory
 10 Division at CERN, where part of this research was carried
 11 out and to the Walter Greiner Gesellschaft zur Förderung der
 12 physikalischen Grundlagenforschung e.V. through the Carl
 13 W. Fueck Laureatus Chair.

APPENDIX

A. VERTICAL AND HORIZONTAL VORTICITY

In the main text we have illustrated how, at late times, the evolution of the ratio of the EM energy in the poloidal and toroidal components converges to a constant value $E_{\text{EM}}^{\text{tor}} \approx E_{\text{EM}}^{\text{pol}}/2$ (see Fig. 4). In what follows we provide a number of elements to explain this result. To this scope, we use Fig. 5, to show for the four binaries considered the spatial distribution of the absolute value of the (rest-mass) density-weighted kinematic vorticity. We recall that the kinematic vorticity is defined as

$$\omega_{\perp}^{xy} := h_{\mu}^x h_{\nu}^y \omega^{\mu\nu}, \quad (\text{A1})$$

where $\omega_{\mu\nu}$ and $h_{\mu\nu} := g_{\mu\nu} + u_{\mu} u_{\nu}$ are the vorticity and projector tensor orthogonal to the fluid four-velocity u^{μ} , respectively (Rezzolla & Zanotti 2013). Figure 5 reports the “vertical vorticity”, i.e., the weighted vorticity $|\rho\omega_{\perp}^{xz}|$ in the polar plane (top row) and the “horizontal vorticity”, i.e., $|\rho\omega_{\perp}^{xy}|$ in the equatorial planes (bottom row). Since the vorticity tensor has all components being nonzero, the split in vertical and horizontal vorticity is, to some extent, arbitrary. However, such simple split helps to understand the evolution of the growth rates in the toroidal and poloidal components. Indeed, the strength of $|\rho\omega_{\perp}^{xy}|$ and $|\rho\omega_{\perp}^{xz}|$ can be taken as proxies for the strength of $\gamma_{\text{tol}}^{\text{pol}}$ and γ_{pol} , respectively.

The selected snapshots correspond to the times when the growth rate of the poloidal EM energy reaches its maximum, and in all cases these times occur for $t_{\text{sh},1/2} > t > t_{\text{mer}}$. While at these times the vertical vorticity is comparable to the horizontal vorticity, earlier on in the shearing (not shown in Fig. 5), the vorticity is mostly horizontal as the high-density regions of the two stars have not yet come into contact and the shear develops mostly with the low-density regions of the two stars. Indeed, a vertical vorticity is hardly present in the early-shear stages of the DD and IR binaries, so that for these binaries the growth rate of the toroidal component is significantly higher than that of the poloidal one (see also Fig. 1). At the times depicted in Fig. 5, and also subsequently, the vertical vorticity will develop further as the collision of the high-density regions squeezes and moves upward the matter compressed by the colliding stellar cores. Hence, the poloidal component of the EM energy will experience an exponential growth immediately after $t = t_{\text{mer}}$.

This dichotomy in the development of the turbulence, i.e., mostly horizontal at early times but then also vertical at later times (especially for the DD and IR binaries), and the corresponding anisotropy in the turbulence distribution, is washed out at later times, when the turbulence becomes increasingly isotropic. This is possible because the magnetic feedback on the matter dynamics remains negligible, since

the amplifying field is still relatively weak ($\sim 10^{11}\text{--}10^{13}$ G). The reaching of an isotropic turbulence such that the strength of magnetic field is equally distributed in all the components (topological equipartition), provides then the natural explanation for the energy hierarchy expressed by Eq. (1) and represented in the top panel of Fig. 4.

B. COMPARING XCFC-GWRR WITH FULL GENERAL RELATIVITY

The use of an approximate gravity solver – based on xCFC approximation and combined with GWRR terms – is what allowed us to perform calculations at high resolution and affordable computational costs. Clearly, it is essential to establish what is the error that such approximation introduces and this can be easily done when comparing with a full general-relativistic simulations performed at a low-resolution of 300 m. Figure 6 shows the evolution of the maximum of the conserved rest-mass density (Rezzolla & Zanotti 2013), $D^* := \rho W \psi^6$ for 2.5 ms after merger [here ψ is the conformal factor in the xCFC formulation (Jiang et al. 2025)], comparing results from BHAC+ with GWRR (solid lines), and FLL (dashed lines) for all the binaries simulated. To show the importance of the GWRR corrections, we show the evolution without such terms (dotted line) in the case of the IR binary (top panel). Note the considerable differences that emerge for $t - t_{\text{mer}} > 1.5$ ms.

Despite the fundamental differences between the constrained-evolution scheme with CFC and the constraint-damping Z4 scheme, the two codes show an agreement that is overall very good. Only a slight phase difference of approximately 0.1–0.2 ms develops over time, and in BHAC+ the two stellar cores collide slightly earlier (by ~ 0.05 ms), which we attribute to the metric initialisation under the CFC approximation. Across the four test cases, the average relative differences range from $\sim 3\%$ to 12% , while the maximum deviations lie between approximately 10% and 25%. We should note that this is a very critical test for the xCFC-GWRR scheme, which was shown to be very accurate in the post-merger phase, when the remnant and the spacetime have reached an approximate axisymmetry (Jiang et al. 2025). The dominant source of discrepancy arises from the GWRR treatment, which corrects the GW energy and angular-momentum loss in the xCFC scheme up to 2.5 PN order but only in the lapse function, leaving the shift vector and the non-diagonal components of the spatial metric unchanged (Jiang et al. 2025). It should also be emphasised that differences of this order (or even larger) have been reported between the post-merger evolution computed when employing different but fully general relativistic codes (Espino et al. 2023).

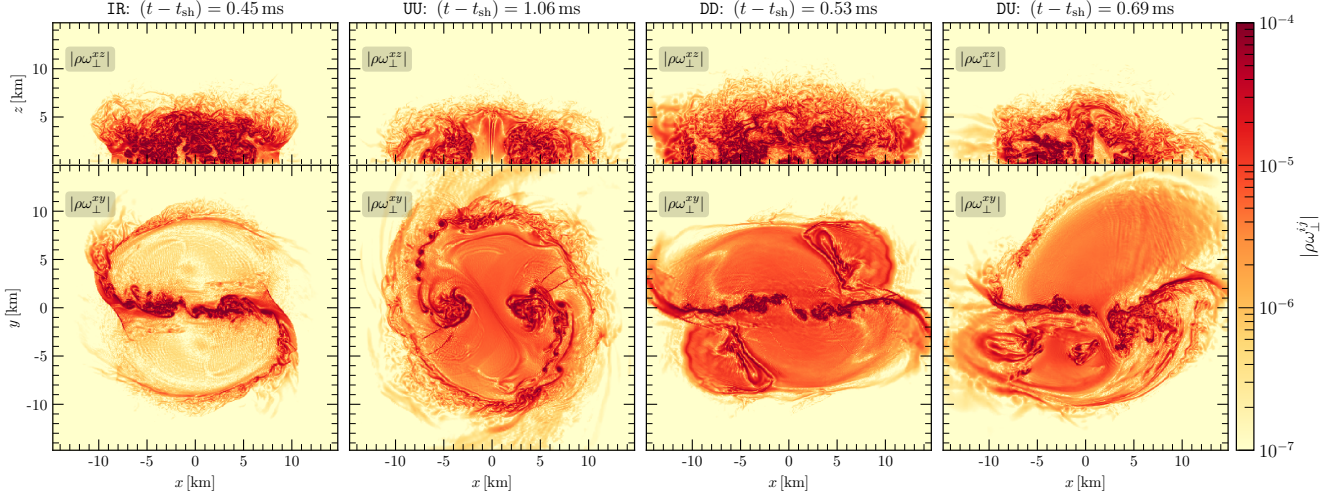


Figure 5. Absolute values of density-weighted kinematic vorticity $|\rho\omega_{\perp}^{ij}|$ for all cases at the time when the growth rate of poloidal EM energy reach their peaks. The top and bottom rows show the distributions of $|\rho\omega_{\perp}^{xz}|$ and $|\rho\omega_{\perp}^{xy}|$ on the (x, z) and (x, y) planes, respectively. The different columns refer to the four binaries considered and at four representative times. The distributions are rotated so as to highlight the different distributions of vorticity.

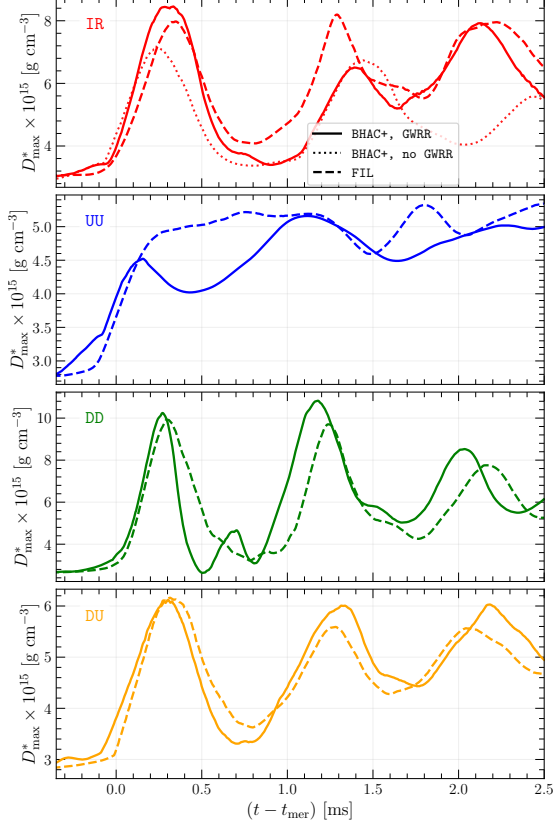


Figure 6. Time evolution of the maximum of the conserved rest-mass density from simulations using **FIL** (dashed lines) and **BHAC+**, either without GWRR terms (dotted lines) or with them included. Note the importance of the latter in reproducing the results of overall dynamics comparing to the full numerical-relativity simulations. In all cases, the finest spatial resolution is of 300 m resolution.

One may be concerned that the differences in kinetic and thermal energies introduced by the approximate gravity treatment could influence the onset and development of turbulence. However, because the fraction of kinetic energy converted into EM energy is only $\sim 1\%$, the observed relative differences of $\lesssim 10\%$ remain largely subdominant over the resolution-induced errors that govern the dynamics of the KHI.

As a final comment, we note that to minimise the computational costs, we follow the strategy of [Jiang et al. \(2025\)](#) and optimise the ratio $\chi := \Delta t_{\text{met}}/\Delta t_{\text{MHD}}$, where Δt_{met} is the interval between two metric updates and Δt_{MHD} is the MHD timestep. Since the relative difference between BHAC and FIL solutions reduces to $\lesssim 0.5\%$ for $\Delta t_{\text{met}} \leq 5 \times 10^{-2} M_{\odot}$, we adopt $\Delta t_{\text{met}} = 5 \times 10^{-2} M_{\odot}$ as the upper bound. This reduces the computational costs considerably and provides a substantial benefit in high-resolution runs where Δt_{MHD} becomes very small.

REFERENCES

Abbott, B. P., Abbott, R., Abbott, T. D., et al. 2017, Phys. Rev. Lett., 119, 161101, doi: [10.1103/PhysRevLett.119.161101](https://doi.org/10.1103/PhysRevLett.119.161101)

Acker, F., B. de R. Borges, R., & Costa, B. 2016, J. Comput. Phys., 313, 726, doi: [10.1016/j.jcp.2016.01.038](https://doi.org/10.1016/j.jcp.2016.01.038)

Aguilera-Miret, R., Christian, J.-E., Rosswog, S., & Palenzuela, C. 2025, Mon. Not. Roy. Astron. Soc., 3067, 3077, doi: [10.1093/mnras/staf1291](https://doi.org/10.1093/mnras/staf1291)

Aguilera-Miret, R., Palenzuela, C., Carrasco, F., Rosswog, S., & Viganò, D. 2024, Phys. Rev. D, 110, 083014, doi: [10.1103/PhysRevD.110.083014](https://doi.org/10.1103/PhysRevD.110.083014)

Aguilera-Miret, R., Viganò, D., & Palenzuela, C. 2022, Astrophys. J. Lett., 926, L31, doi: [10.3847/2041-8213/ac50a7](https://doi.org/10.3847/2041-8213/ac50a7)

Alic, D., Bona-Casas, C., Bona, C., Rezzolla, L., & Palenzuela, C. 2012, Phys. Rev. D, 85, 064040, doi: [10.1103/PhysRevD.85.064040](https://doi.org/10.1103/PhysRevD.85.064040)

Baiotti, L., Giacomazzo, B., & Rezzolla, L. 2008, Phys. Rev. D, 78, 084033, doi: [10.1103/PhysRevD.78.084033](https://doi.org/10.1103/PhysRevD.78.084033)

Baiotti, L., & Rezzolla, L. 2017, Rept. Prog. Phys., 80, 096901, doi: [10.1088/1361-6633/aa67bb](https://doi.org/10.1088/1361-6633/aa67bb)

Bamber, J., Tsokaros, A., Ruiz, M., & Shapiro, S. L. 2024, Phys. Rev. D, 110, 024046, doi: [10.1103/PhysRevD.110.024046](https://doi.org/10.1103/PhysRevD.110.024046)

Bauswein, A., & Stergioulas, N. 2015, Phys. Rev. D, 91, 124056, doi: [10.1103/PhysRevD.91.124056](https://doi.org/10.1103/PhysRevD.91.124056)

Bernuzzi, S., & Hilditch, D. 2010, Phys. Rev. D, 81, 084003, doi: [10.1103/PhysRevD.81.084003](https://doi.org/10.1103/PhysRevD.81.084003)

Blanchet, L. 2014, Living Reviews in Relativity, 17, 2, doi: [10.12942/lrr-2014-2](https://doi.org/10.12942/lrr-2014-2)

Bonazzola, S., & Gourgoulhon, E. 1996, Astron. and Astrophys., 312, 675

Bovard, L., Martin, D., Guercilena, F., et al. 2017, Phys. Rev. D, 96, 124005. <https://arxiv.org/abs/1709.09630>

Bucciantini, N., & Del Zanna, L. 2011, Astron. Astrophys., 528, A101, doi: [10.1051/0004-6361/201015945](https://doi.org/10.1051/0004-6361/201015945)

Celora, T., Palenzuela, C., Viganò, D., & Aguilera-Miret, R. 2025. <https://arxiv.org/abs/2505.01208>

Chabanov, M., Tootle, S. D., Most, E. R., & Rezzolla, L. 2023, Astrophys. J. Lett., 945, L14, doi: [10.3847/2041-8213/acbbc5](https://doi.org/10.3847/2041-8213/acbbc5)

Chen, R.-C., Zhang, B.-B., Wang, C.-W., et al. 2025, Nature Astronomy, doi: [10.1038/s41550-025-02649-w](https://doi.org/10.1038/s41550-025-02649-w)

Cheong, P. C.-K., Foucart, F., Ng, H. H.-Y., et al. 2025, Phys. Rev. D, 111, 043036, doi: [10.1103/PhysRevD.111.043036](https://doi.org/10.1103/PhysRevD.111.043036)

Cheong, P. C.-K., Lam, A. T.-L., Ng, H. H.-Y., & Li, T. G. F. 2021, Monthly Notices of the Royal Astronomical Society, 508, 2279, doi: [10.1093/mnras/stab2606](https://doi.org/10.1093/mnras/stab2606)

Chi-Kit Cheong, P., Tsokaros, A., Ruiz, M., et al. 2024, arXiv e-prints, arXiv:2409.10508, doi: [10.48550/arXiv.2409.10508](https://doi.org/10.48550/arXiv.2409.10508)

Ciolfi, R. 2020, Monthly Notices of the Royal Astronomical Society: Letters, 495, L66, doi: [10.1093/mnrasl/slaa062](https://doi.org/10.1093/mnrasl/slaa062)

Combi, L., & Siegel, D. M. 2023, Astrophys. J., 944, 28, doi: [10.3847/1538-4357/acac29](https://doi.org/10.3847/1538-4357/acac29)

Combi, L., & Siegel, D. M. 2023, Phys. Rev. Lett., 131, 231402, doi: [10.1103/PhysRevLett.131.231402](https://doi.org/10.1103/PhysRevLett.131.231402)

Cook, W., Gutiérrez, E. M., Bernuzzi, S., et al. 2025. <https://arxiv.org/abs/2508.19342>

Cordero-Carrión, I., Cerdá-Durán, P., Dimmelmeier, H., et al. 2009, Phys. Rev. D, 79, 024017, doi: [10.1103/PhysRevD.79.024017](https://doi.org/10.1103/PhysRevD.79.024017)

Dimmelmeier, H., Font, J. A., & Müller, E. 2002, Astron. Astrophys., 388, 917

Dudi, R., Dietrich, T., Rashti, A., et al. 2022, Phys. Rev. D, 105, 064050, doi: [10.1103/PhysRevD.105.064050](https://doi.org/10.1103/PhysRevD.105.064050)

Espino, P. L., Bozzola, G., & Paschalidis, V. 2023, Phys. Rev. D, 107, 104059, doi: [10.1103/PhysRevD.107.104059](https://doi.org/10.1103/PhysRevD.107.104059)

Etienne, Z. B., Paschalidis, V., Haas, R., Mösta, P., & Shapiro, S. L. 2015, Class. Quantum Grav., 32, 175009, doi: [10.1088/0264-9381/32/17/175009](https://doi.org/10.1088/0264-9381/32/17/175009)

Faye, G., & Schäfer, G. 2003, Phys. Rev. D, 68, 084001, doi: [10.1103/PhysRevD.68.084001](https://doi.org/10.1103/PhysRevD.68.084001)

Fermi-LAT Collaboration. 2017, ArXiv e-prints. <https://arxiv.org/abs/1710.05450>

Fields, J., Radice, D., & Hammond, P. 2025. <https://arxiv.org/abs/2507.18695>

Frieben, J., & Rezzolla, L. 2012, Mon. Not. R. Astron. Soc., 427, 3406, doi: [10.1111/j.1365-2966.2012.22027.x](https://doi.org/10.1111/j.1365-2966.2012.22027.x)

Fujibayashi, S., Kiuchi, K., Wanajo, S., et al. 2023, Astrophys. J., 942, 39, doi: [10.3847/1538-4357/ac9ce0](https://doi.org/10.3847/1538-4357/ac9ce0)

Giacomazzo, B., Rezzolla, L., & Baiotti, L. 2009, Mon. Not. R. Astron. Soc., 399, L164, doi: [10.1111/j.1745-3933.2009.00745.x](https://doi.org/10.1111/j.1745-3933.2009.00745.x)

—. 2011, Phys. Rev. D, 83, 044014, doi: [10.1103/PhysRevD.83.044014](https://doi.org/10.1103/PhysRevD.83.044014)

Giacomazzo, B., Zrake, J., Duffell, P. C., MacFadyen, A. I., & Perna, R. 2015, Astrophys. J., 809, 39, doi: [10.1088/0004-637X/809/1/39](https://doi.org/10.1088/0004-637X/809/1/39)

Gottlieb, O., Metzger, B. D., Foucart, F., & Ramirez-Ruiz, E. 2025, Astrophys. J., 984, 77, doi: [10.3847/1538-4357/adc577](https://doi.org/10.3847/1538-4357/adc577)

Gottlieb, O., et al. 2023, Astrophys. J. Lett., 954, L21, doi: [10.3847/2041-8213/aceeff](https://doi.org/10.3847/2041-8213/aceeff)

Gutiérrez, E. M., Cook, W., Radice, D., et al. 2025. <https://arxiv.org/abs/2506.18995>

Hajela, A., Margutti, R., Alexander, K. D., et al. 2019, Astrophys. J. Lett., 886, L17, doi: [10.3847/2041-8213/ab5226](https://doi.org/10.3847/2041-8213/ab5226)

Hajela, A., Margutti, R., Bright, J. S., et al. 2022, Astrophys. J. Lett., 927, L17, doi: [10.3847/2041-8213/ac504a](https://doi.org/10.3847/2041-8213/ac504a)

Harten, A., Lax, P. D., & van Leer, B. 1983, SIAM Rev., 25, 35, doi: [10.1137/1025002](https://doi.org/10.1137/1025002)

Hessels, J. W., Ransom, S. M., Stairs, I. H., et al. 2006, *Science*, 311, 1901, doi: [10.1126/science.1123430](https://doi.org/10.1126/science.1123430)

Jiang, J.-L., Ng, H. H.-Y., Chabanov, M., & Rezzolla, L. 2025, *Phys. Rev. D*, 111, 103043, doi: [10.1103/PhysRevD.111.103043](https://doi.org/10.1103/PhysRevD.111.103043)

Karakas, B., Matur, R., & Ruffert, M. 2025, *Mon. Not. R. Astron. Soc.*, doi: [10.1093/mnras/staf2009](https://doi.org/10.1093/mnras/staf2009)

Kawaguchi, K., Fujibayashi, S., Domoto, N., et al. 2023, arXiv preprint arXiv:2306.06961

Kawamura, T., Giacomazzo, B., Kastaun, W., et al. 2016, *Phys. Rev. D*, 94, 064012, doi: [10.1103/PhysRevD.94.064012](https://doi.org/10.1103/PhysRevD.94.064012)

Keppens, R., Teunissen, J., Xia, C., & Porth, O. 2021, *Computers & Mathematics with Applications*, 81, 316

Kiuchi, K. 2024, arXiv preprint arXiv:2405.10081

Kiuchi, K., Cerdá-Durán, P., Kyutoku, K., Sekiguchi, Y., & Shibata, M. 2015, *Phys. Rev. D*, 92, 124034, doi: [10.1103/PhysRevD.92.124034](https://doi.org/10.1103/PhysRevD.92.124034)

Kiuchi, K., Reboul-Salze, A., Shibata, M., & Sekiguchi, Y. 2024, *Nature Astronomy*, 8, 298, doi: [10.1038/s41550-024-02194-y](https://doi.org/10.1038/s41550-024-02194-y)

Lyman, J. D., Lamb, G. P., Levan, A. J., et al. 2018, *Nature Astronomy*, doi: [10.1038/s41550-018-0511-3](https://doi.org/10.1038/s41550-018-0511-3)

Metzger, B. D. 2017, *Living Reviews in Relativity*, 20, 3, doi: [10.1007/s41114-017-0006-z](https://doi.org/10.1007/s41114-017-0006-z)

Most, E. R., Jens Papenfort, L., Dexheimer, V., et al. 2020, *European Physical Journal A*, 56, 59, doi: [10.1140/epja/s10050-020-00073-4](https://doi.org/10.1140/epja/s10050-020-00073-4)

Most, E. R., Papenfort, L. J., & Rezzolla, L. 2019, *Mon. Not. R. Astron. Soc.*, 490, 3588, doi: [10.1093/mnras/stz2809](https://doi.org/10.1093/mnras/stz2809)

Most, E. R., Peterson, J., Scurto, L., Pais, H., & Dexheimer, V. 2025, *Astrophys. J. Lett.*, 989, L29, doi: [10.3847/2041-8213/adf62d](https://doi.org/10.3847/2041-8213/adf62d)

Most, E. R., & Quataert, E. 2023, *Astrophys. J. Lett.*, 947, L15, doi: [10.3847/2041-8213/acca84](https://doi.org/10.3847/2041-8213/acca84)

Mösta, P., Radice, D., Haas, R., Schnetter, E., & Bernuzzi, S. 2020, *Astrophys. J. Lett.*, 901, L37, doi: [10.3847/2041-8213/abb6ef](https://doi.org/10.3847/2041-8213/abb6ef)

Musolino, C., Rezzolla, L., & Most, E. R. 2025, *Astrophys. J. Lett.*, 984, L61, doi: [10.3847/2041-8213/adcd6d](https://doi.org/10.3847/2041-8213/adcd6d)

Neuweiler, A., et al. 2025. <https://arxiv.org/abs/2510.14850>

Ng, H. H.-Y., Cheong, P. C.-K., Lin, L.-M., & Li, T. G. F. 2021, *The Astrophysical Journal*, 915, 108, doi: [10.3847/1538-4357/ac0141](https://doi.org/10.3847/1538-4357/ac0141)

Ng, H. H.-Y., Jiang, J.-L., Musolino, C., et al. 2024, *Phys. Rev. D*, 109, 064061, doi: [10.1103/PhysRevD.109.064061](https://doi.org/10.1103/PhysRevD.109.064061)

Ng, H. H.-Y., Musolino, C., Tootle, S. D., & Rezzolla, L. 2025, *Astrophys. J. Lett.*, 985, L36, doi: [10.3847/2041-8213/add324](https://doi.org/10.3847/2041-8213/add324)

Oechslin, R., Janka, H.-T., & Marek, A. 2007, *Astron. Astrophys.*, 467, 395, doi: [10.1051/0004-6361:20066682](https://doi.org/10.1051/0004-6361:20066682)

Olivares, H., Porth, O., Davelaar, J., et al. 2019, *Astron. Astrophys.*, 629, A61, doi: [10.1051/0004-6361/201935559](https://doi.org/10.1051/0004-6361/201935559)

Ott, C. D., Dimmelmeier, H., Marek, A., et al. 2007, *Class. Quantum Grav.*, 24, 139, doi: [10.1088/0264-9381/24/12/S10](https://doi.org/10.1088/0264-9381/24/12/S10)

Palenzuela, C., Aguilera-Miret, R., Carrasco, F., et al. 2022, *Phys. Rev. D*, 106, 023013, doi: [10.1103/PhysRevD.106.023013](https://doi.org/10.1103/PhysRevD.106.023013)

Papenfort, L. J., Tootle, S. D., Grandclément, P., Most, E. R., & Rezzolla, L. 2021, arXiv e-prints, arXiv:2103.09911. <https://arxiv.org/abs/2103.09911>

Paschalidis, V. 2017, *Classical and Quantum Gravity*, 34, 084002, doi: [10.1088/1361-6382/aa61ce](https://doi.org/10.1088/1361-6382/aa61ce)

Porth, O., Olivares, H., Mizuno, Y., et al. 2017, *Computational Astrophysics and Cosmology*, 4, 42, doi: [10.1186/s40668-017-0020-2](https://doi.org/10.1186/s40668-017-0020-2)

Price, D. J., & Rosswog, S. 2006, *Science*, 312, 719, doi: [10.1126/science.1125201](https://doi.org/10.1126/science.1125201)

Radice, D., Bernuzzi, S., & Perego, A. 2020, *Annual Review of Nuclear and Particle Science*, 70, 95, doi: [10.1146/annurev-nucl-013120-114541](https://doi.org/10.1146/annurev-nucl-013120-114541)

Radice, D., Galeazzi, F., Lippuner, J., et al. 2016, *Mon. Not. R. Astron. Soc.*, 460, 3255, doi: [10.1093/mnras/stw1227](https://doi.org/10.1093/mnras/stw1227)

Rasio, F. A., & Shapiro, S. L. 1999, *Class. Quantum Grav.*, 16, R1

Rezzolla, L., Giacomazzo, B., Baiotti, L., et al. 2011, *Astrophys. J. Letters*, 732, L6, doi: [10.1088/2041-8205/732/1/L6](https://doi.org/10.1088/2041-8205/732/1/L6)

Rezzolla, L., & Zanotti, O. 2013, *Relativistic Hydrodynamics* (Oxford University Press), doi: [10.1093/acprof:oso/9780198528906.001.0001](https://doi.org/10.1093/acprof:oso/9780198528906.001.0001)

Ruiz, M., Shapiro, S. L., & Tsokaros, A. 2018, *Phys. Rev. D*, 98, 123017, doi: [10.1103/PhysRevD.98.123017](https://doi.org/10.1103/PhysRevD.98.123017)

Ruiz, M., Tsokaros, A., & Shapiro, S. L. 2020, arXiv e-prints, arXiv:2001.09153. <https://arxiv.org/abs/2001.09153>

Schnetter, E., Hawley, S. H., & Hawke, I. 2004, *Class. Quantum Grav.*, 21, 1465, doi: [10.1088/0264-9381/21/6/014](https://doi.org/10.1088/0264-9381/21/6/014)

Siegel, D. M., Ciolfi, R., Harte, A. I., & Rezzolla, L. 2013, *Phys. Rev. D*, 87, 121302, doi: [10.1103/PhysRevD.87.121302](https://doi.org/10.1103/PhysRevD.87.121302)

Steinhoff, J., Hinderer, T., Dietrich, T., & Foucart, F. 2021, *Phys. Rev. Res.*, 3, 033129, doi: [10.1103/PhysRevResearch.3.033129](https://doi.org/10.1103/PhysRevResearch.3.033129)

The LIGO Scientific Collaboration, & The Virgo Collaboration. 2017, *Phys. Rev. Lett.*, 119, 161101, doi: [10.1103/PhysRevLett.119.161101](https://doi.org/10.1103/PhysRevLett.119.161101)

Togashi, H., Nakazato, K., Takehara, Y., et al. 2017, *Nucl. Phys.*, A961, 78, doi: [10.1016/j.nuclphysa.2017.02.010](https://doi.org/10.1016/j.nuclphysa.2017.02.010)

Tootle, S. D., Papenfort, L. J., Most, E. R., & Rezzolla, L. 2021, *Astrophys. J. Lett.*, 922, L19, doi: [10.3847/2041-8213/ac350d](https://doi.org/10.3847/2041-8213/ac350d)

Yip, A. K. L., & Li, T. G. F. 2025. <https://arxiv.org/abs/2509.10150>

Yoshida, S. 2012, *Phys. Rev. D*, 86, 104055, doi: [10.1103/PhysRevD.86.104055](https://doi.org/10.1103/PhysRevD.86.104055)

Zhu, J.-P., Yang, Y.-P., Zhang, B., Gao, H., & Yu, Y.-W. 2022, *Astrophys. J.*, 938, 147, doi: [10.3847/1538-4357/ac8e60](https://doi.org/10.3847/1538-4357/ac8e60)

Zhu, Z., Li, A., & Rezzolla, L. 2020, *Phys. Rev. D*, 102, 084058, doi: [10.1103/PhysRevD.102.084058](https://doi.org/10.1103/PhysRevD.102.084058)